

# Advancing Plain Vision Transformer Towards Remote Sensing Foundation Model

Di Wang, Qiming Zhang, Yufei Xu, Jing Zhang, *Member, IEEE*, Bo Du, *Senior Member, IEEE*, Dacheng Tao, *Fellow, IEEE* and Liangpei Zhang, *Fellow, IEEE*

**Abstract**—Large-scale vision foundation models have made significant progress in visual tasks on natural images, where the vision transformers are the primary choice for their good scalability and representation ability. However, the utilization of large models in the remote sensing (RS) community remains under-explored where existing models are still at small-scale, which limits the performance. In this paper, we resort to plain vision transformers with about 100 million parameters and make the first attempt to propose large vision models customized for RS tasks and explore how such large models perform. Specifically, to handle the large image size and objects of various orientations in RS images, we propose a new rotated varied-size window attention to substitute the original full attention in transformers, which could significantly reduce the computational cost and memory footprint while learn better object representation by extracting rich context from the generated diverse windows. Experiments on detection tasks demonstrate the superiority of our model over all state-of-the-art models, achieving 81.16% mAP on the DOTA-V1.0 dataset. The results of our models on downstream classification and segmentation tasks also demonstrate competitive performance compared with the existing advanced methods. Further experiments show the advantages of our models on computational complexity and few-shot learning. The code and models will be released at <https://github.com/ViTAE-Transformer/Remote-Sensing-RVSA>.

**Index Terms**—Vision Transformer, Remote Sensing, Object Detection, Scene Classification, Semantic Segmentation.

## I. INTRODUCTION

THE geoinformatics community is vigorously developing by combining with computer technologies because of the necessity for human production, and the most representative achievement is the “4D product” including digital Line graphic, digital elevation model, digital raster graphic, and digital orthophoto map (DOM). Among these productions, the remote sensing image (RSI) is the dominant data source for



Fig. 1. The comparison between (a) natural images and (b) RSIs. Here, we show some common categories including bridge and airplane in both types of images. Compared with the natural images from horizontal observation, RSIs tend to be in an overhead view. The natural images are from the ImageNet-1K dataset, while the RSIs are chosen from the UCM, AID, or NWPU datasets.

generating the DOM since it is easy to access and can be obtained in real-time. The RSIs are being employed in many valuable applications such as scene recognition for land use and land cover classification for precision agriculture [1], [2] and object detection for maritime monitoring [3].

It is necessary to effectively represent the RSI contents and attributes to perform the above applications. In the current remote sensing (RS) field, the convolutional neural networks (CNNs) are the most commonly used models for extracting hierarchical multiscale visual features. However, existing studies [4], [5] reveal that the limited receptive field of convolution in each layer makes it difficult for CNNs to pay attention to long-range pixels and extract global context. To address this issue, the self-attention (SA) mechanism [6] is proposed to obtain flexible global dependency by enabling the interaction between arbitrary pixels in images, delivering promising results in the computer vision (CV) field. Further, vision transformer [7] adopts the design of multi-head SA (MHSA), which simultaneously implements the above procedure in multiple projected subspaces, which diversifies the extracted contexts and improves the feature representation.

The plain vision transformer (ViT) [7] is a very simple architecture that stacks several transformer encoder blocks sequentially after the patch embedding layer, where features after each block are at the same scale. To better adapt the vision transformers to downstream tasks, researchers borrow the idea of hierarchical design in CNNs and devise hierarchical vision transformers accordingly [8], [9]. These models are usually pretrained in a supervised way using large-scale datasets and finetuned on the downstream tasks. The recent work [10] empirically studies the hierarchical vision transformers for RSIs by comparing different pretraining strategies and

D. Wang, Q. Zhang and Y. Xu contributed equally to this paper. (*Corresponding author: Bo Du*)

D. Wang and B. Du are with the School of Computer Science, Wuhan University, Wuhan 430072, China (e-mail: wd74108520@gmail.com; dubo@whu.edu.cn). B. Du is also with the National Engineering Research Center for Multimedia Software and Institute of Artificial Intelligence, Wuhan University, Wuhan 430072, China.

Q. Zhang, Y. Xu and J. Zhang are with the School of Computer Science, Faculty of Engineering, The University of Sydney, Australia (e-mail: qzha2506@uni.sydney.edu.au; yuxu7116@uni.sydney.edu.au; jing.zhang1@sydney.edu.au).

D. Tao is with the JD Explore Academy, China and is also with the School of Computer Science, Faculty of Engineering, The University of Sydney, Australia (e-mail: dacheng.tao@gmail.com).

L. Zhang is with the State Key Laboratory of Information Engineering in Surveying, Mapping and Remote Sensing, Wuhan University, Wuhan 430079, China (e-mail: zlp62@whu.edu.cn).

different models. It confirms the superiority of hierarchical vision transformers over CNNs and reveals the effectiveness of pretraining with RS scene datasets like MillionAID [11]. Nevertheless, due to the strong presentation ability of the transformers, researchers question the necessity of the hierarchical design in transformers for downstream tasks. Thanks to the development of the unsupervised learning in masked image modeling (MIM) [12], recent work reveals that such a pretraining process can give a good initialization for plain ViTs to achieve surprising results on various downstream tasks including object detection and pose estimation [13], [14]. For example, ViTDet [13] uses intermediate features at the same scale and upsamples/downsamples them to build the feature pyramid for object detection. The main insight behind their success is that the multiscale prior can be learned from the data during the pretraining, thus making it possible to discard the hierarchical structure.

Inspired by the above pilot studies, we employ the same MIM pretraining and finetuning routine to investigate the influences of plain ViTs on RS tasks. Usually, obtaining the annotations is expensive and nontrivial since understanding RSIs usually requires some expert experience. By contrast, it is much easier to obtain massive unlabeled RSIs in different resolutions and temporals from different kinds of sensors, e.g., via the abundant satellites for continuous earth observations. How to leverage the abundant unlabeled RSIs for pretraining has become an active research topic in the RS community. A few self-supervised learning (SSL) methods [15], [16] have been proposed, which however only target CNNs and have not been proven effective for large-scale vision transformer models. Recently, reconstruction-based SSL methods such as MAE [12] have been proposed and shown effective for pretraining plain ViTs and adapting them for downstream tasks [13], [14]. In this paper, we also employ MAE to pretrain the plain ViT and the recently proposed ViTAE transformer with about 100M parameters on the MillionAID dataset without using the labels.

After pretraining, we adapt the vision transformers to downstream tasks via finetuning on the corresponding datasets. To reduce the computational cost and memory footprint, a natural choice is to replace the full self-attention with local window attention [13]. However, the windows are in fixed sizes and locations, which may restrict the region to extract useful context and limit the model representation ability. A recently proposed method named varied-size attention (VSA) [17] addresses this issue by learning trainable scaling factors and offset to adapt the size, shape, and location of windows to diverse image content, thus delivering better performance on many tasks. However, RSIs are different from natural images in capturing objects from different view directions because of the gravity-free environment caused by the overhead view as shown in Figure 1. To handle this difference, we propose to extend VSA to rotated varied-size attention (RVSA). It introduces an extra learnable rotation mechanism in determining the window configuration, where oriented windows at different angles, sizes, shapes, and locations are obtained to extract richer context. We evaluate the proposed method on both plain ViT [7] and ViTAE [9] models for three kinds of

RS tasks including scene classification, semantic segmentation, and object detection. We hope this study can fill the gap and provide useful insights about developing large plain vision transformers for the RS community.

The main contribution of this study is three-fold:

- (1) We demonstrate the possibility of pretraining plain ViTs with about 100 million parameters on RSIs, adapting them for downstream RS tasks, and delivering competitive performance. To our best knowledge, they are so far the largest models in the remote sensing community, making a step towards the remote sensing foundation model.
- (2) We introduce a learnable rotation mechanism into the vision transformer to learn varied-size windows with different orientation angles for attention calculation, which is very suitable to deal with RSIs. It promotes the extraction of rich context from the generated windows and learning better feature representation.
- (3) Experimental results show that the proposed models set new state-of-the-art (SOTA) on the detection task, and obtain competitive performances on classification and segmentation tasks. Besides, we also show the advantages of the proposed models in terms of computational complexity and few-shot learning ability.

The remainder of this paper is organized as follows. Section II briefly reviews related works including vision foundation models, window-based vision transformers, and model pretraining for RS tasks. Section III describes the proposed method, where we separately present the implementation of unsupervised MAE pretraining on MillionAID and the proposed RVSA method. The experiment results on the three tasks and the related comprehensive analyses are presented in section IV. Finally, Section V concludes this paper.

## II. RELATED WORK

### A. Vision Foundation Model

Foundation models based on transformers have demonstrated strong capabilities and exciting homogeneity in both vision and language tasks [18], [19]. Vision transformers have also experienced rapid development towards large-scale foundation models thanks to their great potential in scalability and structure flexibility, e.g., the model size can be easily scaled up via stacking the same transformer layers with widening dimension [20], introducing a mixture of experts [21], and introducing inductive bias [9], [22], [23]. Among them, plain ViT structures have attracted more attention for their simplicity and flexibility in input formats and superior performance in natural image classification tasks [24]. However, how to adapt the plain ViTs with isotropic structures to downstream visual tasks remains challenging. Recently, ViTDet [13] demonstrates that although there is no multi-stage structure in plain ViTs, they can generate multi-scale features via simple up- and down-sampling modules and use the window-attention mechanism to reduce computational cost and memory footprint significantly. Similarly, ViTPose [14] shows the potential of the plain structure on pose estimation tasks with a simpler decoder. Inspired by their success, we argue it is also of great

significance to explore the potential of the plain ViT structures in RS tasks, which has been largely ignored. In this work, we develop the first plain ViT backbone networks for remote sensing tasks and scale them up to 100M parameters, which are the largest models in remote sensing literature. Equipped with the proposed RVSA method, they show superior performance on different RS tasks including classification, detection, and segmentation.

### B. Window-based Vision Transformer

Although the plain ViTs demonstrate superior performance with model scaling, the full attention operation employed in them brings quadratic complexities over the image size, limiting their applications in downstream visual tasks where high-resolution images are very common. To address this issue, window-based MHSA (WMHSA) [8] has been employed by partitioning the images into non-overlapping windows and conducting MHSA inside each window. WMHSA has linear computational complexity with respect to the image size, making it possible to process high-resolution images. For example, ViTDet [13] explores interleaved windows-based and full attention modules to process images with sizes up to  $1,024 \times 1,024$ . Although the success of WMHSA in balancing memory consumption and performance, it needs extra mechanisms to bridge the connection between different windows, e.g., shifting operations or full attentions. To alleviate such an issue, some works introduce different window partitions with the connection between adjacent windows or additional tokens for cross-window information exchange [25], [26]. Despite their efficiency in different vision tasks, they rely on hand-crafted designs of the window shape and size as well as sequentially stack these layers for modeling relationships between distant tokens. Recently, VSA [17] proposes to learn adaptive window size in a data-driven manner, where the windows could cover different regions and promote cross-window information exchange. In this work, we extend the VSA idea to adapt the plain ViT for remote sensing tasks. Specifically, to better adapt the vision transformer to remote images, we propose the RVSA method by introducing a learnable rotation mechanism. Such a strategy provides network-oriented windows at different angles, sizes, shapes, and locations to learn better object representation. The orientation-aware mechanism improves the performance of vision transformers on different RS tasks.

### C. Model Pretraining for RS task

Model pretraining is an essential step to improve the performance of deep neural networks on RSIs. Previous methods mostly utilize ImageNet [27] dataset for pretraining and obtain performance improvement in classification, detection, and segmentation with task-specific designs [28]–[30]. Unfortunately, due to the huge difference between natural images and RSIs, there always exist domain gaps to be mitigated when transferring these models pretrained on natural images to the remote sensing tasks. Recently, [10] proposes to pretrain deep models on a large-scale RS dataset named MillionAID in a fully-supervised manner. It demonstrates that the pretraining on RS

datasets can help improve the performance of both CNNs and vision transformers. However, the requirement of more labeled data is still a burden for pretraining much larger models. To break the labeled data insufficiency restriction, RS representations from other resources are explored. For example, GeoKR [31] leverages the land cover ratio in the digital geographical information product as a weak label for RS representation learning. However, the shift of label distribution between data from different resources still impedes the learning. Some works resort to self-supervised learning [12], [32]–[34] with different RS characteristics taken into the design, e.g., exploring seasonal variants for constructing positive pairs [15] or leveraging spatial and temporal information [16]. However, they only target CNNs. A very recent method RingMo [35] employs an advanced MiM method named SimMiM [36] to pretrain large-scale vision transformer models. Different from these works, we use the representative MAE method [12] for MIM pretraining and specifically focus on advancing plain ViTs for remote sensing tasks.

## III. PROPOSED METHOD

In this section, we will first introduce the details about the unsupervised pretraining of plain ViT and ViTAE with MAE and the design of the proposed RVSA modules. Then, we will briefly discuss how to transfer the pretrained models to different RS tasks.

### A. Unsupervised Pretraining by MAE

To explore the effectiveness of MIM pretraining in remote sensing tasks, we pretrain our model using MAE [12] with the large-scale RSI dataset, i.e., MillionAID [11]. In the following, we will briefly introduce the dataset, the MAE method, the network structure used during pretraining, and corresponding implementation details.

1) *MillionAID*: The MillionAID dataset [11] is a large-scale dataset with RS scene images and corresponding labels. It contains 100,0848 non-overlapping RS scenes in RGB formats, which is suitable to serve as inputs for typical deep vision models. There are 51 classes in the dataset, where each class has about 2,000~45,000 images. MillionAID is collected from Google Earth, where images are captured with diverse sensors and thus have different resolutions. Generally, the image sizes in the MillionAID dataset range from  $110 \times 110$  to  $31,672 \times 31,672$ . It should be noted that although the MillionAID dataset contains both images and labels, we only use the images during pretraining and discard the labels by following the unsupervised pretraining routine.

2) *MAE*: MAE [12] aims to recover the masked image parts given the visible ones with an encoder-decoder structure. Specifically, for an input image, it tokenizes the image by first splitting the image into non-overlapping patches and then projecting each patch into a visual token using a patch embedding layer. After that, several visual tokens are dropped from the inputs and treated as masked regions to be predicted, following a pre-defined mask ratio. The remained tokens are fed into the transformer encoder for feature extraction. Then, several learnable mask tokens and the extracted features of

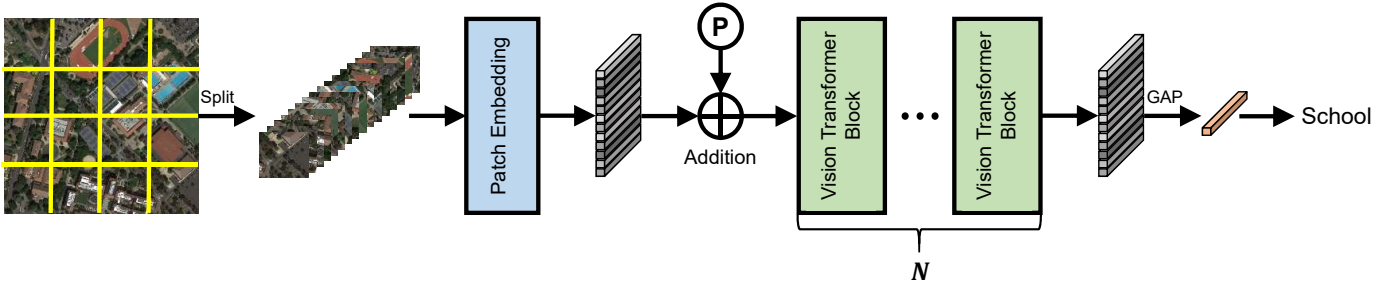


Fig. 2. Overall structure of the pretrained vision transformer network. “P” means the positional encoding. The final output tokens are averaged using global average pooling (GAP) for classification.

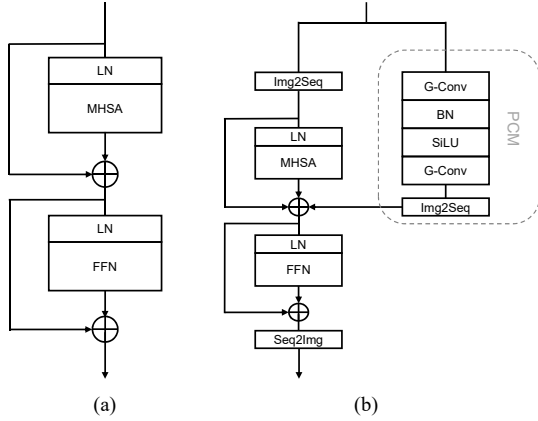


Fig. 3. The structures of the adopted blocks in the MAE encoder. (a) ViT block. (b) Modified ViTAE normal cell. Here, BN, LN, and FFN are batch normalization layer, layer normalization layer, and feed-forward network, G-Conv means the group convolutional layer. Img2Seq and Seq2Img are the reshape operation for conducting transformation between 1-D and 2-D features, these functions are not necessary for pretraining since there are only 1-D token sequences.

visible tokens are processed by the transformer decoder to recover the masked regions. During training, the model is optimized to minimize the distance between the recovered regions and the ground truth masked regions, either in pixel space or feature space. We follow the original MAE setting and calculate the loss in the normalized pixel space. For more details about MAE, please refer to [12].

3) *Pretrained Backbone Networks*: One key design in MAE is token dropping, which greatly accelerates the training speed and reduces the memory footprint during pretraining. Besides, the random dropping mechanism can improve the spatial diversity of the remained tokens. However, this operation will break the spatial relationship between tokens. Such a limitation makes it unsuitable in pretraining networks with 2D-specific designs, such as window attention operations and 2D down-sampling layers. To this end, operations that do not take 2D prior into consideration are more beneficial in MAE pretraining tasks, e.g., the vanilla full self-attention layers or convolution layers with  $1 \times 1$  kernel size.

Following the above analysis, we adopt two backbone networks for pretraining in the paper, i.e., plain ViT [7] and ViTAE [37]. The former one is composed of plain transformer encoders with full self-attention layers. This simple structure enables it to seamlessly work with the MAE pretraining since

it discards the 2D structures and directly treats the image as a 1D sequence. The latter one incorporates inductive bias such as locality from convolutions along with the full self-attention layers, i.e., employing parallel convolution branches (PCM) along with the MHSA layers. However, it is difficult to directly adopt the ViTAE structure for MAE pretraining since the random masking strategy breaks the spatial relationship while ViTAE uses  $3 \times 3$  convolutions in PCM. To address this issue, there are small modifications to PCM, i.e., we adopt convolution with kernel size  $1 \times 1$  in PCM during pretraining. After that, the kernel size is padded to  $3 \times 3$  when finetuning on specific downstream tasks. Assuming the weight in pretraining for  $i$ th convolutional layer is  $\mathbf{W}_F^{(i)} = [\theta]_{1 \times 1}$  (ignoring the channel space), the padded kernel is implemented as follows

$$\mathbf{W}_F^{(i)} = \begin{bmatrix} \alpha & \alpha & \alpha \\ \alpha & \theta & \alpha \\ \alpha & \alpha & \alpha \end{bmatrix}_{3 \times 3}, \quad (1)$$

where  $\theta$  is the learned value during MAE and  $\alpha$  is initialized to 0 and is learnable during finetuning. Besides, we adopt a shallow design of the PCM in the utilized ViTAE model, i.e., a convolutional layer, a batch normalization layer, a SiLU layer, and a convolutional layer in sequence, to save the memory footprint. Figure 3 shows the plain transformer block and the basic ViTAE block used for MAE pretraining. To mitigate the issue of lack of position information in ViTAE, a sin-cos positional encoding is added after the patch embedding layer to emphasize the positional information (Figure 3 has not shown for simplicity). More details can be referred to [9], [37].

We utilize the “base” version of the ViT and ViTAE models both with about 100M parameters. The networks are denoted as “ViT-B” and “ViTAE-B”, respectively. The detailed structures of the two networks can be found in Table I, where “Patch Size” represents the size of split patches and “Embedding Dim” is the dimension of the projected tokens. “Head” denotes the number of heads used in MHSA. “Group” represents the number of groups for the convolutions in PCM, which is not used in the ViT-B model. “Ratio” means the expansion ratio of the FFN. “Depth” represents the number of transformer blocks in the two models. It has the same meaning with  $N$  as demonstrated in Figure 2.

4) *Implementation Details*: We utilize two subsets  $S_1$  and  $S_2$  during pretraining. The two subsets have 949,848 and 51,000 images, respectively. They are randomly sampled from

TABLE I  
HYPER-PARAMETER SETTINGS OF ViT-B AND ViTAE-B.

Network	ViT-B [37]	ViTAE-B [9]
Patch Size	16	16
Embedding Dim	768	768
Head	12	12
Group	—	192
Ratio	4	4
Depth	12	12

TABLE II  
RESULTS OF DIFFERENT HYPER-PARAMETER SETTINGS IN MAE FOR PRETRAINING ViT-B ON THREE DATASETS, I.E., UCM, AID, AND NWPU. “AVG” DENOTES THE AVERAGE TOP-1 ACCURACY ON THREE DATASETS.

Top1 Acc (%)	UCM-55	AID-28	NWPU-19	AVG
Mask Ratio = 0.6 Epoch = 400				
Linear probe	45.81	57.51	59.03	54.12
Fine tune	99.62	97.22	94.05	96.96
Mask Ratio = 0.75 Epoch = 400				
Linear probe	49.90	61.70	61.28	57.63
Fine tune	99.71	97.06	94.43	97.07
Mask Ratio = 0.9 Epoch = 400				
Linear probe	51.71	58.61	61.22	57.18
Fine tune	99.43	96.33	93.86	96.54
Mask Ratio = 0.75 Epoch = 1600				
Linear probe	51.24	62.20	61.75	58.40
Fine tune	99.62	97.53	94.56	97.24

the MillionAID dataset. Note that a class-balance sampling strategy is employed in constructing  $S_2$ , i.e., we randomly select 1,000 images from each category. During pretraining, we use a batch size of 2048, equally distributed on 8 A100 GPUs, with the AdamW [38] optimizer. The models are trained for 1,600 epochs if not specified, following the default setting in MAE [12].

Due to the huge distribution difference between the natural images and remote sensing images, we first investigate the optimal mask ratio in MAE for RSIs. To this end, we search for the optimal mask ratio on the  $S_1$  dataset for pretraining. We utilize a linear probing setting and finetuning setting for evaluation. For the linear probing setting, we randomly initialize a linear classifier after the backbone and only update the classifier’s parameters during training. The models are trained for 100 epochs with a batch size of 256. For the finetuning setting, parameters from the backbone network and the classifier are together tuned with a layer-wise learning rate decay mechanism [12], [39]. Except the batch size is set to 64 and the epoch of 200. The evaluation is conducted on existing RS scene classification tasks, including UCM [40], AID [41], and NWPU [42] datasets, by finetuning the pretrained models on the three datasets. The models are pretrained for 400 epochs and finetuned for 200 epochs, respectively. The results are available in Table II. We report the average accuracy on the three evaluation datasets (denoted as “AVG”). It can be observed that with the mask ratio of 0.75, the pretrained models obtain the best performance in both linear probing and finetuning settings. In the following experiments, we set the mask ratio to 0.75 by default. In addition, it can be seen that the performance could be improved when a longer training schedule is used, e.g., 1600 epochs. In the following experiments, all the pretrained models are obtained by training for 1600 epochs.

## B. Finetuning with Rotated Varied-Size Attention

Different from natural images, images from RS tasks usually have larger resolutions. It will cause unaffordable training costs when directly transferring the pretrained models with full self-attention on the downstream tasks, due to the quadratic computational complexity of full self-attention. To this end, we substitute the full self-attention modules with window-based attention modules during the finetuning stage, which reduces the computational complexity to linear with respect to the image size. This substitution is also seamless since the difference between the two kinds of attention lies in the manner of attention calculation, which is parameter-free. However, the original window-based attention operations always take fixed-size window partitions and at a fixed orientation. Due to the gravity-free nature of objects in the remote sensing images, it is probably not the optimal design to use fixed-size window partitions. To address this issue, we design the rotated varied size window attention mechanism, which will be described in detail as follows.

1) *Window-based attention and Varied-size window attention: Window-based attention* We will briefly review the window-based attention [8] and varied-size window attention (VSA) [17] in this part. Given an input  $\mathbf{X} \in \mathbb{R}^{C \times H \times W}$ , window-based attention firstly partitions the input  $\mathbf{X}$  into several non-overlapping windows, i.e.,  $\mathbf{X}_w \in \mathbb{R}^{C' \times s \times s}$ , where  $s$  represents the size of the window. There are a total of  $\frac{H}{s} \times \frac{W}{s}$  windows in the image. Then, features inside each window is transformed to  $h$  triplets representing the query, key and value features:  $\{\mathbf{Q}_w^{(i)}, \mathbf{K}_w^{(i)}, \mathbf{V}_w^{(i)}\}_{i=1}^h$  by three linear layers, respectively, where  $\mathbf{Q}_w^{(i)}, \mathbf{K}_w^{(i)}, \mathbf{V}_w^{(i)} \in \mathbb{R}^{C' \times s \times s}$ ,  $C' = hC'$ , and  $h$  is the number of heads in the attention layers. We denote the generated features as  $\{\mathbf{Q}_w^{(i,j)}, \mathbf{K}_w^{(i,j)}, \mathbf{V}_w^{(i,j)}\}_{j=1, \dots, \frac{HW}{s^2}}^h$ , where  $j$  indexes the window. After that, the attention calculations are conducted inside each window, i.e.,

$$\begin{aligned} \mathbf{F}_w^{(i,j)} &= SA(\mathbf{Q}_w^{(i,j)}, \mathbf{K}_w^{(i,j)}, \mathbf{V}_w^{(i,j)}) \\ &= \text{softmax}\left(\frac{\mathbf{Q}_w^{(i,j)} \mathbf{K}_w^{(i,j)T}}{\sqrt{C'}}\right) \mathbf{V}_w^{(i,j)}, \end{aligned} \quad (2)$$

where  $\mathbf{F}_w^{(i,j)} \in \mathbb{R}^{s^2 \times C'}$ . Then, the features from different heads are concatenated along the channel dimension and features from different windows are concatenated along the spatial dimension to recover the shape of the input feature.

**Varied-size window attention** However, such a fixed-size window partition method may be probably not optimal in tasks with the need to deal with objects of various sizes. Recently, VSA is proposed to mitigate this issue by learning the window size in a data-driven manner. Specifically, it treats the fixed-size windows as initialization and extracts the query features from these windows, i.e.,  $\mathbf{Q}_w$ . For key and value features, the input  $\mathbf{X}_w$  are used to estimate an offset and scale of the target window

$$S_w, O_w = \text{Linear}(\text{LeakyReLU}(\text{GAP}(\mathbf{X}_w))), \quad (3)$$

where  $S_w$  and  $O_w$  represent the scaling factor and the offset of the target window. *GAP* is short for the global average pooling

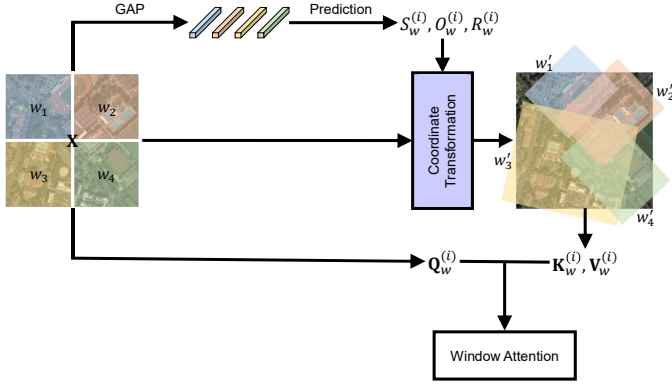


Fig. 4. The pipeline of the proposed RVSA method in the  $i$ -th attention head.  $w_*$  denotes the predicted windows for sampling key and value tokens.

operation. Then, the initial window is transformed according to the estimated two factors, i.e.,

$$\begin{bmatrix} x_l \\ y_l \\ x_r \\ y_r \end{bmatrix} = \begin{bmatrix} x^c \\ y^c \\ x^c \\ y^c \end{bmatrix} + \begin{bmatrix} x_l^r \\ y_l^r \\ x_r^r \\ y_r^r \end{bmatrix}, \quad (4)$$

$$\begin{bmatrix} x'_l \\ y'_l \\ x'_r \\ y'_r \end{bmatrix} = \begin{bmatrix} x^c \\ y^c \\ x^c \\ y^c \end{bmatrix} + \begin{bmatrix} o_x \\ o_y \\ o_x \\ o_y \end{bmatrix} + \begin{bmatrix} x_l^r \cdot s_x \\ y_l^r \cdot s_y \\ x_r^r \cdot s_x \\ y_r^r \cdot s_y \end{bmatrix}, \quad (5)$$

where  $x_l, y_l, x_r, y_r$  represent the coordinates of the left upper and right down corners of the initial window.  $x_c, y_c$  represent the center coordinate of the window, and  $x_l^r, y_l^r, x_r^r, y_r^r$  are the distance between the corner points and the center in horizontal and vertical directions, respectively.  $o_x, o_y$  and  $s_x, s_y$  denote the predicted offsets and scale factors, i.e.,  $S_w = \{s_x, s_y \in \mathbb{R}^1\}, O_w = \{o_x, o_y \in \mathbb{R}^1\}$ .  $x'_l, y'_l, x'_r, y'_r$  indicate the corners of the transformed window. Then, the key and value features are sampled from the transformed windows and used for attention calculation. The number of sampled key and value tokens are the same as the query tokens to maintain the same computational complexity between the VSA and window-based attention.

2) *Rotated Varied-Size Attention*: VSA successfully demonstrates its effectiveness in computer vision tasks on natural images. However, there are significant differences between natural images and RSIs. For example, due to the gravity-free nature of objects in RSIs, they may present at arbitrary angles in the images, while the default windows and the windows generated by VSA are always in the horizontal and vertical directions, which is probably not optimal for RS tasks. To this end, we introduce one extra dimension to control the orientation of the windows, leading to the rotated varied size attention technique in this paper. Specifically, the rotation angle  $\Theta_w = \{\theta \in \mathbb{R}^1\}$  is predicted along with  $S_w$  and  $O_w$ , given the input feature  $\mathbf{X}_w$ , i.e.,

$$S_w, O_w, \Theta_w = \text{Linear}(\text{LeakyReLU}(\text{GAP}(\mathbf{X}_w))), \quad (6)$$

and the transformed coordinates are calculated as:

$$\begin{bmatrix} x'_{l/r} \\ y'_{l/r} \end{bmatrix} = \begin{bmatrix} x^c \\ y^c \end{bmatrix} + \begin{bmatrix} o_x \\ o_y \end{bmatrix} + \begin{bmatrix} \cos \theta & \sin \theta \\ -\sin \theta & \cos \theta \end{bmatrix} \begin{bmatrix} x^r_{l/r} \cdot s_x \\ y^r_{l/r} \cdot s_y \end{bmatrix}. \quad (7)$$

Figure 4 shows a diagram of the proposed RVSA method.

We also propose a variant of RVSA, which allows that key and values tokens can be samples from different windows, i.e., we use separate prediction layers to predict the scale, shift, and rotation factors for key and values tokens, respectively:

$$\begin{aligned} S_w^K, O_w^K, \Theta_w^K &= \text{Linear}_K(\text{LeakyReLU}(\text{GAP}(\mathbf{X}_w))), \\ S_w^V, O_w^V, \Theta_w^V &= \text{Linear}_V(\text{LeakyReLU}(\text{GAP}(\mathbf{X}_w))). \end{aligned} \quad (8)$$

This more flexible module is denoted as RVSA $^\diamond$ .

3) *Computational Complexity Analysis*: We analyze the computational complexity of the proposed RVSA module. Given the input  $\mathbf{X} \in \mathbb{R}^{C \times H \times W}$ , we first partition the input into non-overlapping windows with shape  $s \times s$ . Since the complexity is the same for the calculation of each window, we will demonstrate the computational complexity of one window in this section. The features inside the window are used to predict the scale, shift, and rotation factors of the window, with a subsequent global average pooling (GAP) layer, an activation layer, and a linear layer. The GAP layer brings a computational complexity of  $\mathcal{O}(s^2C)$ . The activation layers bring about zero computations and we dismiss them for simplicity. The following linear layer projects the pooled features from dimension  $C$  to dimension  $5h$ , since it needs to predict two scales and shift factors in horizontal and vertical directions and one rotation factor for each head. Thus, the linear projection layer has  $\mathcal{O}(5hC)$  computational complexity. After that, bilinear sampling is used to sample the key and value tokens from the transformed windows, which has about  $\mathcal{O}(4s^2C)$  computational complexity. Thus, the total computational complexity of RVSA for each window is  $\mathcal{O}(5s^2C + 5hC)$ . There are a total number of  $\frac{HW}{s^2}$  windows after the window partition. To this end, the overall extra computational complexity brought by RVSA is  $\mathcal{O}(5HWC(1 + \frac{5h}{s^2}))$ . Since the computational complexity of the original window attention is  $\mathcal{O}(2s^2HWC)$ , where  $s$  is always set to 7 and  $h$  is set to 12, RVSA only brings marginally extra (i.e., about 11%) computational cost.

4) *Implementation Details*: To adapt the MAE pretrained models to downstream RS tasks, we replace the plain MHSA modules with the proposed RVSA modules. Following the strategy in ViTDet [13], we use full attention blocks at each 1/4 depth layer and use RVSA in all other layers. Specifically, for models with 12 layers like the ViT-B and ViTAE-B, we use full attention layers at the 3rd, 6th, 9th, and 12th layer and uses RVSA in all other layers. The modified networks are denoted as “ViT-B + RVSA” and “ViTAE-B + RVSA” in the paper, respectively. Similarly, we use the original window attention, VSA, and RVSA $^\diamond$  for comparison. These variants are denoted as “ViT-B-Win”, “ViT-B + VSA”, “ViT-B + RVSA $^\diamond$ ”, “ViTAE-B-Win”, “ViTAE-B + VSA”, and “ViTAE-B + RVSA $^\diamond$ ”, respectively.

#### IV. EXPERIMENTAL RESULTS

In this section, we evaluate the performance of the proposed models on multiple RS tasks, including scene classification, object detection, and semantic segmentation. We first conduct a series of ablation studies on the object detection task to analyze and find suitable settings for the proposed models. Then, with the help of existing popular frameworks, we compare our methods with the current SOTA approaches on public benchmarks. We also show the superiority of the proposed models in terms of computational complexity (e.g., training speed and memory footprint) and few-shot learning ability.

##### A. Remote Sensing Object Detection

1) *Dataset*: We adopt two challenging large-scale RS oriented bounding box (OBB) detection datasets: DOTA-V1.0 [43] and DIOR-R [44] for evaluation.

- **DOTA-V1.0**: It is the most famous large-scale dataset for OBB detection. It totally contains 2,806 images whose size ranges from  $800 \times 800$  to  $4,000 \times 4,000$ , where 188,282 instances belonging to 15 categories are annotated. The training, validation, and testing sets have 1,411, 458, and 937 images, respectively.
- **DIOR-R**: It is a recently established OBB detection dataset by extending the DIOR [45]. It contains 23,463 images with a total of 192,518 instances. The trainval set and testing set contain 11,725 images with 68,073 instances, and 11,738 images with 124,445 instances, respectively. All images have been cropped to  $800 \times 800$ , where the pixel resolution ranges from 0.5 to 30m. It contains 20 common object categories.

##### 2) Implementation Details and Experimental Settings:

Following the *de facto* standard, all models are trained with the AdamW [38] optimizer, where the learning rate and weight decay are set to  $1e-4$  and  $5e-2$ , respectively. We use the  $1 \times$  training schedule with 12 epochs and a batch size of 2. The learning rate is adjusted by a multi-step scheduler, i.e., the learning rate is reduced by  $10 \times$  at the 8th and 11th epoch. We also adopt the layer-wise learning rate decay strategy, where the decay rate is set to 0.75.

For a fair comparison with [10], we employ the same Oriented R-CNN [46] detection framework for OBB detection while only changing the backbone. We adopt the default hyperparameters defined in OBBDetection<sup>1</sup>. Following ViTDet [13], we separately upsample and downsample the output feature from the last layer through deconvolution and pooling layers to construct the feature pyramid.

Following Oriented R-CNN, when conducting the single-scale training and testing, the DOTA dataset is cropped to  $1,024 \times 1,024$  patches with a stride of 824. We also implement the multiscale training and testing, where the original images are first resized to three scales, i.e., (0.5, 1.0, 1.5), which are then cropped to  $1,024 \times 1,024$  patches with a stride of 524. During training, we adopt the data augmentations including random horizontal and vertical flipping, while the random rotation is considered for multiscale training and testing.

<sup>1</sup><https://github.com/jbwang1997/OBBDetection>

TABLE III  
THE MAP (%) OF ViT-B + RVSA WITH DIFFERENT WINDOW SIZES ON DOTA-V1.0 AND DIOR-R DATASETS.

Window size	4	7	11	14
DOTA-V1.0	77.84	<b>78.75</b>	77.83	77.44
DIOR-R	70.55	<b>70.67</b>	70.40	70.17

TABLE IV  
THE MAP (%) OF DIFFERENT ViT-B VARIANTS ON DOTA-V1.0 AND DIOR-R DATASETS. THE SUFFIX DENOTES DIFFERENT WINDOW ATTENTION METHODS. WA: WINDOW ATTENTION. SF: SCALE FACTOR. OF: OFFSET FACTOR. RF: ROTATION FACTOR.

Method	WA	SF & OF	RF	Oriented R-CNN mAP	
				DOTA-V1.0	DIOR-R
ViT-B				77.05	66.65
ViT-B-Win	✓			77.19	67.95
ViT-B + VSA	✓	✓		78.40	70.48
ViT-B + RVSA	✓	✓	✓	<b>78.75</b>	70.67
ViT-B + RVSA <sup>◇</sup>	✓	✓	✓	78.61	<b>70.85</b>

For DOTA-V1.0, the original training and validation sets are jointly used for training following [10]. We separately evaluate our models on the original testing sets of DOTA-V1.0 and DIOR-R. The evaluation results of DOTA-V1.0 are obtained from the online server by submitting the predictions of the testing set. The average precision (AP) of each class and the mean average precision (mAP) are reported. All experiments are implemented within 2 NVIDIA A100 GPUs.

3) *Determining the Suitable Window Size*: Considering ViTDet [13] and VSA [17] use different window sizes, we first investigate the influence of window size  $s$  on DOTA-V1.0 and DIOR-R. We search for the optimal value of  $s$  in the range of [4, 14] and the results are shown in Table III. Interestingly, the performance peaks at  $s = 7$  on both datasets, and either increasing or decreasing the window size will lead to a performance drop. The reason can be attributed to two aspects. (1) Although a larger window size increases the receptive field and makes the tokens within each window encode more context, it limits the window diversity due to the reduced window number  $\frac{HW}{s^2}$  and thus leads to less-diverse contexts extracted by the model. (2) When decreasing the window size, the number of the attended tokens will also drop, which may result in inefficient information captured during attention. The experiments indicate  $s = 7$  can be a good balance between the token number and window diversity for these RS datasets. Thus we set  $s = 7$  by default in the following experiments.

4) *Comparison of Different Attention Methods*: After determining the window size  $s$ , we compare different attention methods based on ViT-B and the results are listed in Table IV. Surprisingly, ViT-B with full self-attention performs worse than ViT-B-Win despite more tokens involved during attention. By introducing the scale and offset factors, the size and location of the window in VSA can be adaptively learned. Compared with the ViT-B-Win, ViT-B + VSA learns adaptive windows for varied-size objects in different positions, improving the detection performance significantly. Nevertheless, the learned windows are horizontal and vertical, which are insufficient to accurately capture the object context in the

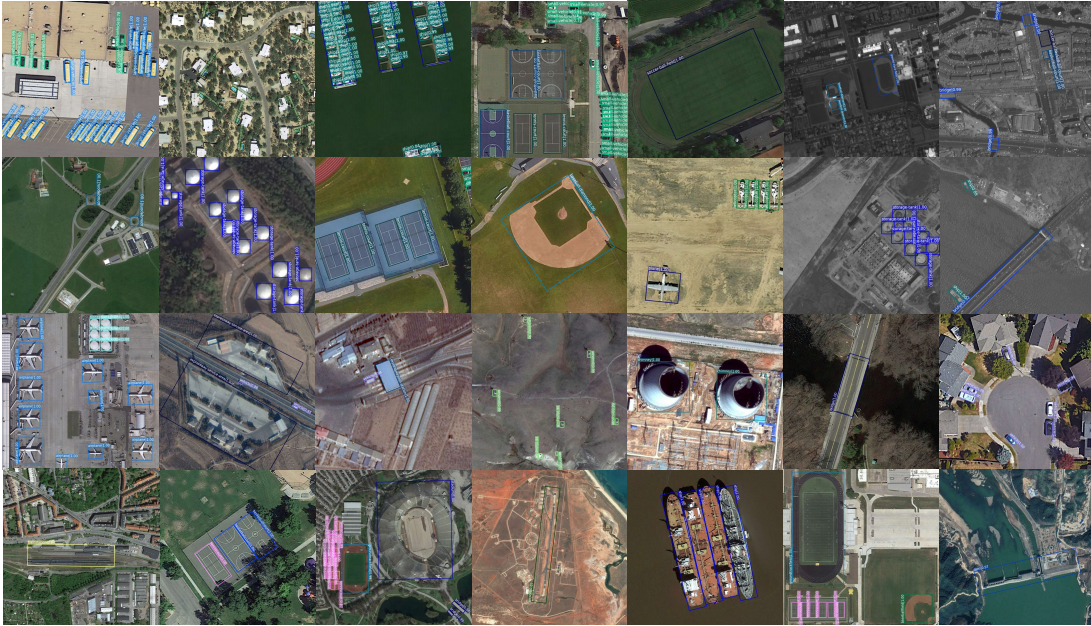


Fig. 5. Some visual detection results. The first two rows are the results of ViTAE-B + RVSA on DOTA-V1.0, while the remained rows are the results of ViTAE-B + RVSA $\diamond$  on DIOR-R. Best viewed with zoom-in.

TABLE V  
THE TRAINING COSTS OF DIFFERENT ViT-B VARIANTS ON DOTA-V1.0 AND DIOR-R DATASETS.

Method	Oriented R-CNN				
	Params (M)	Input Size	FLOPs (G) <sup>1</sup>	Memory (M)	$T_{train}$ (hh:mm:ss)
<b>DOTA-V1.0</b>					
ViT-B <sup>2</sup>	113.73	1,024	717.79	25,757*2	12:30:42
ViT-B-Win	113.63	1,024	427.43	24,685	11:41:29
ViT-B + VSA	113.92	1,024	413.26	25,321	12:12:11
ViT-B + RVSA	114.00	1,024	413.29	25,343	12:31:30
ViT-B + RVSA $\diamond$	114.37	1,024	413.60	25,386	13:08:39
<b>DIOR-R</b>					
ViT-B	112.47	800	364.56	21,408	09:05:08
ViT-B-Win	112.39	800	263.63	12,322	06:12:14
ViT-B + VSA	112.69	800	252.37	12,729	06:56:16
ViT-B + RVSA	112.76	800	252.40	12,744	07:11:35
ViT-B + RVSA $\diamond$	113.13	800	252.48	12,772	07:43:18

<sup>1</sup> The FLOPs are calculated for each backbone network.

<sup>2</sup> This model is trained on 2 GPUs since it encounters the out of memory issue on a single GPU, while other models are trained on a single GPU.

RSI that may be displayed in any direction. ViT-B + RVSA addresses this issue by introducing an extra rotation factor, thus generating windows in various directions to better fit the overhead viewing characteristics in remote sensing. It enables the model to effectively extract contexts that are more suitable for describing RS objects. As a result, ViT-B + RVSA performs better than ViT-B + VSA on both DOTA-V1.0 and DIOR-R. At last, we evaluate ViT-B + RVSA $\diamond$  where the key and value tokens are sampled from different windows to extract contexts more flexibly. Table IV shows that ViT-B + RVSA and ViT-B + RVSA $\diamond$  perform slightly different on the two datasets. We guess that relaxing the constraint that key and value tokens share the same window can further improve the model representation capability while at the risk of overfitting. Therefore, ViT-B + RVSA $\diamond$  performs better on the more challenging dataset DIOR-R, which has more training images and categories.

Besides accuracy, we also compare the training cost of the above models. Table V summarizes the evaluation metrics

including the number of parameters (Params), computations (FLOPs), GPU memory footprint, and training time (shown as  $T_{train}$ ). It can be seen that all these models have more than 100M parameters, where ViT-B has the most memory footprint and FLOPs as well as the longest training time (Note that it uses two GPUs) because of the quadratic complexity of full self-attention. ViT-B-Win alleviates these issues by adopting WMHSA, where the parameters reduce slightly because of the use of relative positional encoding instead of absolute positional encoding. Note that the FLOPs of ViT-B + VSA is smaller than ViT-B-Win since the padding operation is implemented after the generation of query, key, and value tokens. ViT-B + VSA brings slightly extra memory footprints than ViT-B-Win due to learnable scale and offset factors. Compared to ViT-B + VSA, ViT-B + RVSA has a similar complexity, while ViT-B + RVSA $\diamond$  slightly increases the parameters and computational overheads since it adopts individual window prediction layers for key and value tokens. Compared to ViT-B, the proposed ViT-B + RVSA and ViT-B + RVSA $\diamond$  can save approximately half the memory and accelerate the training speed, while achieving better performance.

5) *Compare with State-of-the-art Methods:* We compare the proposed methods with some recently proposed and so far the most advanced methods, and the results are presented in Table VI-VII. The top three scores in each metric are marked by **bold**, **red** and **blue**, respectively. On the DOTA-V1.0 dataset, we list the results of single-scale training and multiscale training, separately. As can be seen, when training on a single scale, our models have advantages in most categories. Concretely, the proposed models perform the best in nine classes and surpass the previous best method by about 1% mAP. In the more competitive multi-scale setting, our models still win the first place in a total of six categories. Owing to the greatly improved detection results in some challenging





TABLE IX  
RESULTS OF DIFFERENT METHODS FOR SCENE CLASSIFICATION.

Pretrain	Backbone	Method	UCM-55	AID-28	AID-55	NWPU-19	NWPU-28
IMP	VGG-16	LSENet [28]	98.53	94.41	96.36	92.23	93.34
IMP	ResNet-50	F <sup>2</sup> BRBM [61]	98.64	96.05	96.97	92.74	94.87
IMP	ResNet-50	GRMANet [62]	99.29	95.43	97.39	93.19	94.72
IMP	ResNet-101	EAM [63]	98.81	94.26	97.06	91.91	94.29
IMP	ResNet-101	MSANet [64]	97.80	93.53	96.01	90.38	93.52
ASP [65]	ResNet-101	—	—	95.40	—	—	94.20
IMP	DenseNet-121	MGM-L-FENet [66]	—	96.45	<b>98.60</b>	92.91	95.39
IMP	MobileNet-V2 [67]	RBFF [68]	95.83	91.02	93.64	84.59	88.05
IMP	ViT-B	—	99.15	93.81	96.08	90.96	93.96
IMP	Swin-T	—	99.43	96.55	98.10	92.73	94.70
CSPT [69]	ViT-B	—	—	96.75	—	—	95.11
CSPT	ViT-L	—	—	96.30	—	—	95.62
RingMo [35]	ViT-B	—	—	96.54	98.38	93.46	95.35
RingMo [35]	Swin-B	—	—	96.90	98.34	<b>94.25</b>	<b>95.67</b>
IMP	ViTAEv2-S	—	99.43	96.61	98.08	93.90	95.29
RSP	ViTAEv2-S	—	<b>99.62</b>	96.91	98.22	<b>94.41</b>	95.60
MAE	ViT-B + RVSA	—	<b>99.70</b>	<b>96.92</b>	98.33	93.79	95.49
MAE	ViT-B + RVSA <sup>◇</sup>	—	<b>99.58</b>	96.86	98.44	93.74	95.45
MAE	ViTAE-B + RVSA	—	99.56	<b>97.03</b>	<b>98.48</b>	<b>93.93</b>	<b>95.69</b>
MAE	ViTAE-B + RVSA <sup>◇</sup>	—	99.50	<b>97.01</b>	<b>98.50</b>	93.92	<b>95.66</b>

TABLE X  
THE DETAILS OF DIFFERENT SEMANTIC SEGMENTATION DATASETS.

Dataset	Training	Validation	Testing	Category	Image Size
Potsdam	24	—	14	6	6,000 × 6,000
iSAID	1411	458	937	15	800 × 800 ~ 4,000 × 13,000
LoveDA	2522	1669	1796	7	1,024 × 1,024

others are for testing. We change the neuron number of the last linear layer to match the number of categories in each dataset. Note that we use the same pretrained models as those in the experiments for object detection and follow the hyperparameter settings in Section III-A4 during finetuning on these datasets. We use the top-1 accuracy as the evaluation metric.

3) *Experimental Results*: Table IX summarizes the scene classification results of different models on the above five settings. It can be seen that our models are superior to other methods in three settings including UCM-55, AID-28, and NWPU-28. These comparison methods include specially designed scene classification methods that use different backbone networks such as ResNet, VGG, DenseNet, and MobileNet, as well as the recently proposed pretraining-based methods with advanced vision transformers. While in other settings, our models still perform to be competitive with RSP-ViTAEv2-S, which is also pretrained on MillionAID. We notice that our methods mainly perform worse in the NWPU-19 setting. It is because the proposed RVSA needs a certain amount of training data to learn the optimal window configurations, while NWPU-19 has relatively small-scale training data. When expanding the training set as in NWPU-28, our models surpass RSP-ViTAEv2-S and achieve the best performance.

### C. Remote Sensing Semantic Segmentation

We also transfer the pretrained models to the semantic segmentation task. Besides the Potsdam<sup>2</sup> and iSAID [70] datasets following [10], we also adopt a recently proposed domain adaptation segmentation dataset — LoveDA [71]. Here, we do not distinguish urban and rural areas, and we directly utilize the official division for general segmentation.

1) *Dataset*: The categories in iSAID are completely the same as DIOR-R since the two datasets share the same set of scenes while targeting different tasks. The details of these datasets for semantic segmentation are shown in Table X.

<sup>2</sup><https://www.isprs.org/education/benchmarks/UrbanSemLab/2d-sem-label-potsdam.aspx>

TABLE XI  
RESULTS OF DIFFERENT METHODS FOR SEMANTIC SEGMENTATION.

Method	Pretrain	Backbone	Potsdam	iSAID	LoveDA
FCN [73]	IMP	VGG-16	85.59	41.70	46.69
DANet [74]	IMP	ResNet-50	89.72	57.50	—
PSPNet [75]	IMP	ResNet-50	89.45	60.30	48.31
DeepLabV3+ [76]	IMP	ResNet-50	89.74	60.80	48.31
Semantic FPN [77]	IMP	ResNet-50	—	59.30	48.15
FarSeg [30]	IMP	ResNet-50	—	63.70	48.15
FactSeg [78]	IMP	ResNet-50	—	<b>64.80</b>	48.94
UNetFormer [79]	IMP	ResNet-18	<b>91.30</b>	—	<b>52.40</b>
UperNet [72]	IMP	ResNet-50	90.64	61.90	51.27
UperNet	IMP	Swin-T	91.17	<b>64.60</b>	50.00
UperNet	RingMo [35]	Swin-B	<b>91.74</b>	<b>67.20</b>	—
UperNet	RSP [10]	ViTAEv2-S	91.21	64.30	<b>53.02</b>
UperNet	MAE	ViT-B + RVSA	90.60	63.76	51.95
UperNet	MAE	ViT-B + RVSA <sup>◇</sup>	90.77	63.85	51.95
UperNet	MAE	ViTAE-B + RVSA	<b>91.22</b>	63.48	52.26
UperNet	MAE	ViTAE-B + RVSA <sup>◇</sup>	91.15	64.49	<b>52.44</b>

2) *Implementation Details and Experimental Settings*: Most of the experimental settings are same with [10]. Considering the more parameters in larger models, we increase the training iterations to 160k. Besides, the layer decay rate is 0.9. Following [8], [10], [37], the UperNet [72] is employed as the segmentation framework. We separately upsample or downsample the outputs from block 4, block 6, block 8, and block12 to form the required feature pyramid as in BeiT [39]. For training on LoveDA, patches of 512 × 512 resolution are randomly cropped from the images as input. We combine the training and validation sets of LoveDA to form a trainval set for training, while the testing set is unchanged. Besides the overall accuracy (OA) computed for the Potsdam dataset following the common protocol in the RS segmentation community, we report the mean of the intersection over union (IoU) for all categories in iSAID and LoveDA. We follow the single scale setting to calculate all metrics for a fair comparison. These experiments are implemented with 2~4 NVIDIA A100 GPUs.

3) *Experimental Results*: Table XI shows the results of different methods. It can be seen that our models obtain comparable performance to SOTA methods. We acknowledge that the performance of the proposed models on the segmentation task is not as impressive as those on the object detection and scene classification tasks. We attribute it to two reasons. First, we only use the classical segmentation framework UperNet, which can not effectively propagate high-level semantics to the high-resolution features. Therefore, it is unable to carry out an accurate pixel-level understanding as the latest proposed frameworks such as UNetFormer [79] and FactSeg [78]. Another reason may be that the vision transformer backbones we adopted have the plain structure whose tokens are directly embedded from 16 × 16 patches and the feature map resolution keeps 1/16 of the input size. Compared with the hierarchical structure like Swin and ViTAEv2, which could generate high-resolution feature maps at early stages, the plain ViTs may lose details, which may be harmful to the pixel-level semantic segmentation task. Nevertheless, the proposed RVSA can still advance the plain ViTs and achieve similar performance to RSP-ViTAEv2-S, demonstrating its strong ability in capturing useful context from the learned rotated varied-size windows.

TABLE XII  
AVERAGE RESULTS ON ALL DATASETS IN EACH TASK.

Model	Detection	Classification	Segmentation
ViT-B	71.85	97.20	67.58
ViT-B + RVSA	74.71	96.84	68.77
ViT-B + RVSA $\diamond$	74.73	96.82	68.86

### D. Comparison with Plain ViT on All Tasks

In this section, we compare the proposed ViT models equipped with RVSA/RVSA $\diamond$  and the plain ViT on all tasks. The plain ViT performs well in the scene classification task but has poor performance on the detection and segmentation tasks. This may be because all tokens probably contribute to the description of the scene category and thus taking all tokens into consideration for attention calculation is beneficial for learning image-level feature representation for scene classification. In contrast, object detection and semantic segmentation prefer object-level and pixel-level feature representation, where the semantics highly relate to the nearby tokens while the tokens far away may contribute less. Thus RVSA and RVSA $\diamond$  could better balance the contribution of nearby and far away tokens and perform much better than the plain ViT on the two tasks. Here, taking ViT-B as an example, we present the average results of different models on all the datasets of different tasks in Table XII. The scores are computed by averaging the metrics across datasets in each task, e.g., the average detection score of ViT-B + RVSA is  $(78.75 + 70.67)/2 \approx 74.71$ . As can be seen, ViT-B with the proposed RVSA modules performs much better than the baseline on detection and segmentation tasks since they promote the extraction of rich contexts from diverse windows. Besides, RVSA and RVSA $\diamond$  perform comparably on the average, although they prefer different datasets at different difficulty levels as shown in Table IX and XI.

### E. Few-shot Learning

Few-shot learning is an important ability of foundation models [9], [80]. To investigate the few-shot learning ability of the proposed models, we conduct the experiments on the DIOR-R datasets using different amounts of training data for object detection. For comparison, we include some small-scale models such as RSP-ResNet-50, RSP-Swin-T, and RSP-ViTAEv2-S, which are trained with all training samples. Their pretrained weights are obtained from the codebase<sup>3</sup>. Figure 6 shows the results. As can be seen, the proposed models outperform the corresponding ViT-B and ViTAE-B baseline models regardless of the number of training samples. In addition, they achieve comparable performance to Swin-T by using only 40% training samples, outperform ResNet-50 and Swin-T when 60% training samples are used, and surpass the strong backbone ViTAEv2-S by using 80% samples. These findings validate the good few-shot learning ability of our models. Figure 6 also shows that RVSA $\diamond$  requires more training samples to perform better than RVSA, as demonstrated in Section IV-A4.

<sup>3</sup><https://github.com/ViTAE-Transformer/ViTAE-Transformer-Remote-Sensing>

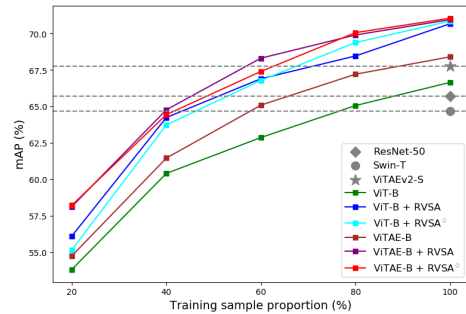


Fig. 6. Results of different models trained with different amounts of training samples on the DIOR-R dataset. The Oriented R-CNN detection framework is adopted for all models.

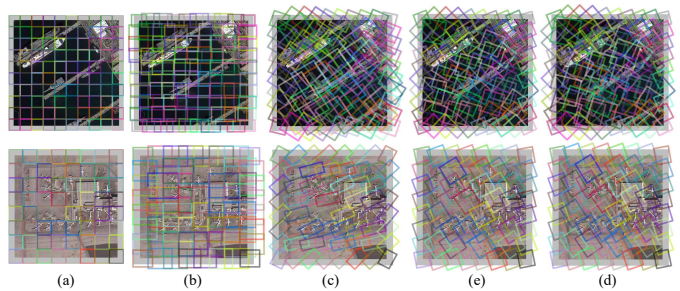


Fig. 7. Visualization of the generated windows of different attention methods based on ViT-B. (a) Window attention. (b) VSA. (c) RVSA. (d) and (e) are the generated windows of RVSA $\diamond$  for the key and value tokens, separately. The images are from the testing sets of DOTA-V1.0 and DIOR-R, respectively.

### F. Visualization of RVSA

Figure 7 shows the visualization results of generated windows from the attention layer in the penultimate block of different models. These models are all based on ViT-B but use different attention methods, including window attention, VSA, RVSA, and RVSA $\diamond$ . The gray areas denote zero paddings such that the feature size can be divisible by the window size. For example, the ViT-B-Win has  $(\frac{1024}{16} + 6)^2 = 100$  windows in one head when processing DOTA-V1.0 images (see the first row in Figure 7 (a)) since zero padding length is 6. As can be seen, the windows generated by VSA can be scaled and shifted to match different objects. Nevertheless, VSA is unable to effectively deal with the arbitrary-oriented objects in RSIs, such as the oriented airplanes in the second row of Figure 7. By contrast, our RVSA introduces the rotation factor to address this issue, obtaining more diverse windows and promoting the extraction of more rich contexts. It is also noteworthy that the generated windows in one head can well adapt to some airplanes and each head can produce a different set of windows. Therefore, the airplanes can be covered by the windows in different heads, implying that RVSA can better deal with arbitrary-oriented objects. Compare with RVSA, RVSA $\diamond$  further improves the flexibility of generated windows. By comparing (d) and (e) with (c), we can find that there are slight changes in the window shape for key and value tokens, which could be useful when dealing with challenging samples and there are a large amount of training data.

## V. CONCLUSION

In this paper, we make the first attempt to investigate the potential of the plain vision transformer towards remote sensing foundation model. Specifically, we propose a novel rotated varied-size window attention method to advance the performance of plain vision transformers. It generates diverse windows at different angles, sizes, shapes, and locations to cover the arbitrary-oriented objects in remote sensing images and enables to extract rich contexts from the generated windows, thereby promoting the learning of better object representation. We validate the proposed method based on the representative unsupervised pretraining method MAE on typical remote sensing tasks including scene classification, object detection, and semantic segmentation. The results demonstrate the superiority of the proposed method and its effectiveness in advancing the plain vision transformer for different tasks. We hope this study could provide useful insights to the community and inspire more future research on developing remote sensing foundation models, especially based on plain vision transformers.

## REFERENCES

- [1] X. Zhang, Y. Sun, K. Shang, L. Zhang, and S. Wang, "Crop classification based on feature band set construction and object-oriented approach using hyperspectral images," *IEEE J. Sel. Topics Appl. Earth Observ. Remote Sens.*, vol. 9, no. 9, pp. 4117–4128, Sep. 2016.
- [2] J. Zhang and D. Tao, "Empowering things with intelligence: a survey of the progress, challenges, and opportunities in artificial intelligence of things," *IEEE Internet of Things Journal*, vol. 8, no. 10, pp. 7789–7817, 2020.
- [3] P. Qin, Y. Cai, J. Liu, P. Fan, and M. Sun, "Multilayer feature extraction network for military ship detection from high-resolution optical remote sensing images," *IEEE J. Sel. Topics Appl. Earth Observ. Remote Sens.*, vol. 14, pp. 11 058–11 069, 2021.
- [4] W. Luo, Y. Li, R. Urtasun, and R. Zemel, "Understanding the effective receptive field in deep convolutional neural networks," in *NeurIPS*, vol. 29, 2016.
- [5] E. Xie, W. Wang, Z. Yu, A. Anandkumar, J. M. Alvarez, and P. Luo, "Segformer: Simple and efficient design for semantic segmentation with transformers," *NeurIPS*, vol. 34, 2021.
- [6] X. Wang, R. Girshick, A. Gupta, and K. He, "Non-local neural networks," in *Proceedings of the IEEE Conference on Computer Vision and Pattern Recognition (CVPR)*, June 2018.
- [7] A. Dosovitskiy, L. Beyer, A. Kolesnikov, D. Weissenborn, X. Zhai, T. Unterthiner, M. Dehghani, M. Minderer, G. Heigold, S. Gelly, J. Uszkoreit, and N. Houlsby, "An image is worth 16x16 words: Transformers for image recognition at scale," *ICLR*, 2021.
- [8] Z. Liu, Y. Lin, Y. Cao, H. Hu, Y. Wei, Z. Zhang, S. Lin, and B. Guo, "Swin transformer: Hierarchical vision transformer using shifted windows," in *ICCV*, 2021, pp. 10 012–10 022.
- [9] Q. Zhang, Y. Xu, J. Zhang, and D. Tao, "Vitaev2: Vision transformer advanced by exploring inductive bias for image recognition and beyond," *arXiv preprint arXiv:2202.10108*, 2022.
- [10] D. Wang, J. Zhang, B. Du, G.-S. Xia, and D. Tao, "An empirical study of remote sensing pretraining," *IEEE Trans. Geosci. Remote Sens.*, pp. 1–1, 2022.
- [11] Y. Long, G.-S. Xia, S. Li, W. Yang, M. Y. Yang, X. X. Zhu, L. Zhang, and D. Li, "On creating benchmark dataset for aerial image interpretation: Reviews, guidances and million-aid," *IEEE J. Sel. Topics Appl. Earth Observ. Remote Sens.*, vol. 14, pp. 4205–4230, 2021.
- [12] K. He, X. Chen, S. Xie, Y. Li, P. Dollár, and R. Girshick, "Masked autoencoders are scalable vision learners," in *CVPR*, June 2022, pp. 16 000–16 009.
- [13] Y. Li, H. Mao, R. Girshick, and K. He, "Exploring plain vision transformer backbones for object detection," *arXiv preprint arXiv:2203.16527*, 2022.
- [14] Y. Xu, J. Zhang, Q. Zhang, and D. Tao, "Vitpose: Simple vision transformer baselines for human pose estimation," 2022.
- [15] O. Mañas, A. Lacoste, X. Giro-i Nieto, D. Vazquez, and P. Rodriguez, "Seasonal contrast: Unsupervised pre-training from uncurated remote sensing data," in *ICCV*, 2021, pp. 9414–9423.
- [16] K. Ayush, B. Uzcent, C. Meng, K. Tanmay, M. Burke, D. Lobell, and S. Ermon, "Geography-aware self-supervised learning," in *ICCV*, 2021, pp. 10 181–10 190.
- [17] Q. Zhang, Y. Xu, J. Zhang, and D. Tao, "Vsa: Learning varied-size window attention in vision transformers," *arXiv preprint arXiv:2204.08446*, 2022.
- [18] J. Devlin, M.-W. Chang, K. Lee, and K. Toutanova, "BERT: Pre-training of Deep Bidirectional Transformers for Language Understanding," *arXiv e-prints*, p. arXiv:1810.04805, Oct. 2018.
- [19] W. Fedus, B. Zoph, and N. Shazeer, "Switch transformers: Scaling to trillion parameter models with simple and efficient sparsity," 2021.
- [20] X. Zhai, A. Kolesnikov, N. Houlsby, and L. Beyer, "Scaling vision transformers," in *CVPR*, June 2022, pp. 12 104–12 113.
- [21] C. Riquelme, J. Puigcerver, B. Mustafa, M. Neumann, R. Jenatton, A. Susano Pinto, D. Keysers, and N. Houlsby, "Scaling vision with sparse mixture of experts," in *NeurIPS*, vol. 34, 2021, pp. 8583–8595.
- [22] Z. Dai, H. Liu, Q. V. Le, and M. Tan, "Coatnet: Marrying convolution and attention for all data sizes," in *NeurIPS*, vol. 34, 2021, pp. 3965–3977.
- [23] Z. Liu, H. Hu, Y. Lin, Z. Yao, Z. Xie, Y. Wei, J. Ning, Y. Cao, Z. Zhang, L. Dong, F. Wei, and B. Guo, "Swin transformer v2: Scaling up capacity and resolution," in *CVPR*, June 2022, pp. 12 009–12 019.
- [24] J. Yu, Z. Wang, V. Vasudevan, L. Yeung, M. Seyedhosseini, and Y. Wu, "Coca: Contrastive captioners are image-text foundation models," *arXiv preprint arXiv:2205.01917*, 2022.
- [25] X. Dong, J. Bao, D. Chen, W. Zhang, N. Yu, L. Yuan, D. Chen, and B. Guo, "Cswin transformer: A general vision transformer backbone with cross-shaped windows," in *CVPR*, June 2022, pp. 12 124–12 134.
- [26] S. Wu, T. Wu, H. Tan, and G. Guo, "Pale transformer: A general vision transformer backbone with pale-shaped attention," in *AAAI*, vol. 36, no. 3, 2022, pp. 2731–2739.
- [27] J. Deng, W. Dong, R. Socher, L.-J. Li, K. Li, and L. Fei-Fei, "Imagenet: A large-scale hierarchical image database," in *CVPR*, 2009, pp. 248–255.
- [28] Q. Bi, K. Qin, H. Zhang, and G.-S. Xia, "Local semantic enhanced convnet for aerial scene recognition," *IEEE Trans. Image Process.*, vol. 30, pp. 6498–6511, 2021.
- [29] J. Ding, N. Xue, Y. Long, G.-S. Xia, and Q. Lu, "Learning roi transformer for oriented object detection in aerial images," in *CVPR*, 2019, pp. 2844–2853.
- [30] Z. Zheng, Y. Zhong, J. Wang, and A. Ma, "Foreground-aware relation network for geospatial object segmentation in high spatial resolution remote sensing imagery," in *CVPR*, 2020, pp. 4095–4104.
- [31] W. Li, K. Chen, H. Chen, and Z. Shi, "Geographical knowledge-driven representation learning for remote sensing images," *IEEE Trans. Geosci. Remote Sens.*, vol. 60, pp. 1–16, 2022.
- [32] T. Chen, S. Kornblith, M. Norouzi, and G. Hinton, "A simple framework for contrastive learning of visual representations," in *ICML*. PMLR, 2020, pp. 1597–1607.
- [33] X. Chen, H. Fan, R. Girshick, and K. He, "Improved baselines with momentum contrastive learning," *arXiv preprint arXiv:2003.04297*, 2020.
- [34] Y. Xu, Q. Zhang, J. Zhang, and D. Tao, "Regioncl: Can simple region swapping contribute to contrastive learning?" *arXiv preprint arXiv:2111.12309*, 2021.
- [35] X. Sun, P. Wang, W. Lu, Z. Zhu, X. Lu, Q. He, J. Li, X. Rong, Z. Yang, H. Chang, Q. He, G. Yang, R. Wang, J. Lu, and K. Fu, "Ringmo: A remote sensing foundation model with masked image modeling," *IEEE Trans. Geosci. Remote Sens.*, pp. 1–1, 2022.
- [36] Z. Xie, Z. Zhang, Y. Cao, Y. Lin, J. Bao, Z. Yao, Q. Dai, and H. Hu, "SimMIM: A Simple Framework for Masked Image Modeling," *arXiv e-prints*, p. arXiv:2111.09886, Nov. 2021.
- [37] Y. Xu, Q. Zhang, J. Zhang, and D. Tao, "Vitaev: Vision transformer advanced by exploring intrinsic inductive bias," *NeurIPS*, vol. 34, 2021.
- [38] I. Loshchilov and F. Hutter, "Decoupled weight decay regularization," in *ICLR*, 2018.
- [39] H. Bao, L. Dong, and F. Wei, "BEiT: BERT Pre-Training of Image Transformers," *arXiv e-prints*, p. arXiv:2106.08254, Jun. 2021.
- [40] Y. Yang and S. Newsam, "Bag-of-visual-words and spatial extensions for land-use classification," in *GEOPROCESSING*, 2010, p. 270–279.
- [41] G.-S. Xia, J. Hu, F. Hu, B. Shi, X. Bai, Y. Zhong, L. Zhang, and X. Lu, "Aid: A benchmark data set for performance evaluation of aerial scene classification," *IEEE Trans. Geosci. Remote Sens.*, vol. 55, no. 7, pp. 3965–3981, 2017.

- [42] G. Cheng, J. Han, and X. Lu, "Remote sensing image scene classification: Benchmark and state of the art," *Proc. IEEE*, vol. 105, no. 10, pp. 1865–1883, 2017.
- [43] G.-S. Xia, X. Bai, J. Ding, Z. Zhu, S. Belongie, J. Luo, M. Datcu, M. Pelillo, and L. Zhang, "Dota: A large-scale dataset for object detection in aerial images," in *CVPR*, June 2018.
- [44] G. Cheng, J. Wang, K. Li, X. Xie, C. Lang, Y. Yao, and J. Han, "Anchor-free oriented proposal generator for object detection," *IEEE Trans. Geosci. Remote Sens.*, vol. 60, pp. 1–11, 2022.
- [45] K. Li, G. Wan, G. Cheng, L. Meng, and J. Han, "Object detection in optical remote sensing images: A survey and a new benchmark," *ISPRS-J. Photogramm. Remote Sens.*, vol. 159, pp. 296–307, 2020.
- [46] X. Xie, G. Cheng, J. Wang, X. Yao, and J. Han, "Oriented r-cnn for object detection," in *ICCV*, October 2021, pp. 3520–3529.
- [47] X. Yang, J. Yan, Z. Feng, and T. He, "R3det: Refined single-stage detector with feature refinement for rotating object," *AAAI*, vol. 35, no. 4, pp. 3163–3171, May 2021.
- [48] Y. Xu, M. Fu, Q. Wang, Y. Wang, K. Chen, G.-S. Xia, and X. Bai, "Gliding vertex on the horizontal bounding box for multi-oriented object detection," *IEEE Trans. Pattern Anal. Mach. Intell.*, vol. 43, no. 4, pp. 1452–1459, 2021.
- [49] G. Cheng, Y. Yao, S. Li, K. Li, X. Xie, J. Wang, X. Yao, and J. Han, "Dual-aligned oriented detector," *IEEE Trans. Geosci. Remote Sens.*, vol. 60, pp. 1–11, 2022.
- [50] J. Han, J. Ding, J. Li, and G.-S. Xia, "Align Deep Features for Oriented Object Detection," *IEEE Trans. Geosci. Remote Sens.*, vol. 60, p. 3062048, Jan. 2022.
- [51] J. Han, J. Ding, N. Xue, and G.-S. Xia, "Redet: A rotation-equivariant detector for aerial object detection," in *CVPR*, June 2021, pp. 2786–2795.
- [52] X. Yang, X. Yang, J. Yang, Q. Ming, W. Wang, Q. Tian, and J. Yan, "Learning high-precision bounding box for rotated object detection via kullback-leibler divergence," in *NeurIPS*, 2021.
- [53] K. H. Wentong Li, Yijie Chen and J. Zhu, "Oriented reppoints for aerial object detection," in *CVPR*, 2022.
- [54] L. Dai, H. Liu, H. Tang, Z. Wu, and P. Song, "Ao2-detr: Arbitrary-oriented object detection transformer," *arXiv preprint arXiv:2205.12785*, 2022.
- [55] X. Yang, J. Yan, M. Qi, W. Wang, Z. Xiaopeng, and T. Qi, "Rethinking rotated object detection with gaussian wasserstein distance loss," in *ICML*, 2021.
- [56] D. Liang, Q. Geng, Z. Wei, D. A. Vorontsov, E. L. Kim, M. Wei, and H. Zhou, "Anchor retouching via model interaction for robust object detection in aerial images," *IEEE Trans. Geosci. Remote Sens.*, vol. 60, pp. 1–13, 2022.
- [57] X. Yang, Y. Zhou, G. Zhang, J. Yang, W. Wang, J. Yan, X. Zhang, and Q. Tian, "The kfiou loss for rotated object detection," *arXiv preprint arXiv:2201.12558*, 2022.
- [58] T.-Y. Lin, P. Goyal, R. Girshick, K. He, and P. Dollár, "Focal loss for dense object detection," in *ICCV*, Oct 2017.
- [59] S. Ren, K. He, R. Girshick, and J. Sun, "Faster r-cnn: Towards real-time object detection with region proposal networks," *IEEE Trans. Pattern Anal. Mach. Intell.*, vol. 39, no. 6, pp. 1137–1149, June 2017.
- [60] S.-B. Chen, Q.-S. Wei, W.-Z. Wang, J. Tang, B. Luo, and Z.-Y. Wang, "Remote sensing scene classification via multi-branch local attention network," *IEEE Trans. Image Process.*, vol. 31, pp. 99–109, 2021.
- [61] X. Zhang, W. An, J. Sun, H. Wu, W. Zhang, and Y. Du, "Best Representation Branch Model for Remote Sensing Image Scene Classification," *IEEE J. Sel. Topics Appl. Earth Observ. Remote Sens.*, vol. 14, pp. 9768–9780, Jan. 2021.
- [62] B. Li, Y. Guo, J. Yang, L. Wang, Y. Wang, and W. An, "Gated Recurrent Multiattention Network for VHR Remote Sensing Image Classification," *IEEE Trans. Geosci. Remote Sens.*, vol. 60, p. 3093914, Jan. 2022.
- [63] Z. Zhao, J. Li, Z. Luo, J. Li, and C. Chen, "Remote Sensing Image Scene Classification Based on an Enhanced Attention Module," *IEEE Geosci. Remote Sens. Lett.*, vol. 18, no. 11, pp. 1926–1930, Nov. 2021.
- [64] G. Zhang, W. Xu, W. Zhao, C. Huang, E. N. Yk, Y. Chen, and J. Su, "A Multiscale Attention Network for Remote Sensing Scene Images Classification," *IEEE J. Sel. Topics Appl. Earth Observ. Remote Sens.*, vol. 14, pp. 9530–9545, Jan. 2021.
- [65] Y. Long, G.-S. Xia, L. Zhang, G. Cheng, and D. Li, "Aerial scene parsing: From tile-level scene classification to pixel-wise semantic labeling," *arXiv preprint arXiv:2201.01953*, 2022.
- [66] Q. Zhao, S. Lyu, Y. Li, Y. Ma, and L. Chen, "Mgml: Multigranularity multilevel feature ensemble network for remote sensing scene classification," *IEEE Trans. Neural Netw. Learn. Syst.*, 2021.
- [67] M. Sandler, A. Howard, M. Zhu, A. Zhmoginov, and L.-C. Chen, "Mobilenetv2: Inverted residuals and linear bottlenecks," in *CVPR*, June 2018.
- [68] M. A. Arefeen, S. T. Nimi, M. Y. S. Uddin, and Z. Li, "A lightweight relu-based feature fusion for aerial scene classification," in *ICIP*, 2021, pp. 3857–3861.
- [69] T. Zhang, P. Gao, H. Dong, Y. Zhuang, G. Wang, W. Zhang, and H. Chen, "Consecutive pretraining: A knowledge transfer learning strategy with relevant unlabeled data for remote sensing domain," *arXiv preprint arXiv:2207.03860*, 2022.
- [70] S. Waqas Zamir, A. Arora, A. Gupta, S. Khan, G. Sun, F. Shahbaz Khan, F. Zhu, L. Shao, G.-S. Xia, and X. Bai, "isaid: A large-scale dataset for instance segmentation in aerial images," in *CVPRW*, 2019, pp. 28–37.
- [71] J. Wang, Z. Zheng, A. Ma, X. Lu, and Y. Zhong, "LoveDA: A remote sensing land-cover dataset for domain adaptive semantic segmentation," in *NeurIPS*, vol. 1, 2021.
- [72] T. Xiao, Y. Liu, B. Zhou, Y. Jiang, and J. Sun, "Unified perceptual parsing for scene understanding," in *ECCV*, 2018, pp. 418–434.
- [73] E. Shelhamer, J. Long, and T. Darrell, "Fully convolutional networks for semantic segmentation," *IEEE Trans. Pattern Anal. Mach. Intell.*, vol. 39, no. 4, pp. 640–651, 2017.
- [74] J. Fu, J. Liu, H. Tian, Y. Li, Y. Bao, Z. Fang, and H. Lu, "Dual attention network for scene segmentation," in *CVPR*, 2019, pp. 3141–3149.
- [75] H. Zhao, J. Shi, X. Qi, X. Wang, and J. Jia, "Pyramid scene parsing network," in *CVPR*, 2017, pp. 6230–6239.
- [76] L.-C. Chen, Y. Zhu, G. Papandreou, F. Schroff, and H. Adam, "Encoder-decoder with atrous separable convolution for semantic image segmentation," in *ECCV*, 2018, pp. 801–818.
- [77] A. Kirillov, R. Girshick, K. He, and P. Dollár, "Panoptic feature pyramid networks," in *CVPR*, 2019, pp. 6392–6401.
- [78] A. Ma, J. Wang, Y. Zhong, and Z. Zheng, "Factseg: Foreground activation-driven small object semantic segmentation in large-scale remote sensing imagery," *IEEE Trans. Geosci. Remote Sens.*, vol. 60, pp. 1–16, 2022.
- [79] L. Wang, R. Li, C. Zhang, S. Fang, C. Duan, X. Meng, and P. M. Atkinson, "Unetformer: A unet-like transformer for efficient semantic segmentation of remote sensing urban scene imagery," *ISPRS-J. Photogramm. Remote Sens.*, vol. 190, pp. 196–214, 2022.
- [80] T. Brown, B. Mann, N. Ryder, M. Subbiah, J. D. Kaplan, P. Dhariwal, A. Neelakantan, P. Shyam, G. Sastry, A. Askell *et al.*, "Language models are few-shot learners," *NeurIPS*, vol. 33, pp. 1877–1901, 2020.